

The UV photodissociation dynamics of ClO radical using velocity map ion imaging

Hahkjoon Kim, Jiho Park, Tracy C. Niday, and Simon W. North^{a)}

Department of Chemistry, Texas A&M University, P.O. Box 30012, College Station, Texas 77842

(Received 3 August 2005; accepted 31 August 2005; published online 28 October 2005)

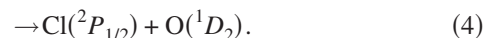
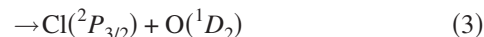
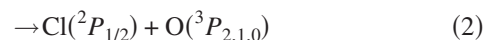
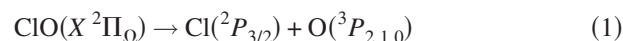
We have studied the wavelength-dependent photodissociation dynamics of jet-cooled ClO radical from 235 to 291 nm using velocity map ion imaging. We find that $\text{Cl}(^2P_{3/2})+\text{O}(^1D_2)$ is the dominant channel above the $\text{O}(^1D_2)$ threshold with minor contributions from the $\text{Cl}(^2P_J)+\text{O}(^3P_J)$ and $\text{Cl}(^2P_{1/2})+\text{O}(^1D_2)$ channels. We have measured the photofragment angular distributions for each dissociation channel and find that the $A\ ^2\Pi$ state reached via a parallel transition carries most of the oscillator strength above the $\text{O}(^1D_2)$ threshold. The formation of $\text{O}(^3P_J)$ fragments with positive anisotropy is evidence of curve crossing from the $A\ ^2\Pi$ state to one of several dissociative states. The curve crossing probability increases with wavelength in good agreement with previous theoretical calculations. We have directly determined the $\text{O}(^1D_2)$ threshold to be $38\,050\pm 20\text{ cm}^{-1}$ by measuring $\text{O}(^1D_2)$ quantum yield in the wavelength range of 260–270 nm. We also report on the predissociation dynamics of ClO below the $\text{O}(^1D_2)$ threshold. We find that the branching ratio of $\text{Cl}(^2P_{3/2})/\text{Cl}(^2P_{1/2})$ is 1.5 ± 0.1 at both 266 and 291 nm. The rotational depolarization of the anisotropy parameters of the $\text{Cl}(^2P_{3/2})$ fragments provides predissociation lifetimes of $1.5\pm 0.2\text{ ps}$ for the 9-0 band and $1.0\pm 0.4\text{ ps}$ for the 8-0 band, in reasonable agreement with previous spectroscopic and theoretical studies. © 2005 American Institute of Physics.

[DOI: 10.1063/1.2083487]

I. INTRODUCTION

The role of photodissociation of chlorine compounds in the stratosphere is critical in understanding stratospheric ozone depletion.¹ Chlorine monoxide is a radical intermediate that plays an important role in the stratospheric ozone depletion via the photodissociation as well as bimolecular reactions.^{2,3} The UV photodissociation of ClO is estimated to be responsible for 2%–3% of the total ozone loss in the stratosphere.⁴ In addition, since ClO is produced as a primary photoproduct of ClONO_2 , an understanding photodissociation dynamics of ClO is critical for modeling recent ClONO_2 photodissociation experiments.^{5,6}

The ClO absorption spectrum is characterized by a continuum that spans from 220 to near 263 nm and the subsequent rovibrational-resolved structure that terminates at 316 nm.⁷ Details of the electronic transitions responsible for the ClO absorption spectrum can be explained considering electronic configurations of ClO. The ground state of ClO has the configuration $(\sigma)^2(\pi)^4(\pi^*)^3(\sigma^*)^0$ and the term symbol $X\ ^2\Pi_\Omega$ which correlates to ground-state atoms. Promotion of an electron from a π orbital to a π^* orbital results in the $(\sigma)^2(\pi)^3(\pi^*)^4(\sigma^*)^0$ configuration and the term symbol $A\ ^2\Pi_\Omega$ and correlates to $\text{Cl}(^2P_J)+\text{O}(^1D_2)$ fragments based on the Wigner-Witmer correlation rule.⁸ There are four electronic pathways for ClO photodissociation which are energetically accessible in the UV region:



Channels (1) and (2) are accessible at wavelengths between 316 and 263 nm and all four channels are accessible at wavelengths shorter than 263 nm. The high-resolution absorption spectrum ClO was first studied by Durie and Ramsay.⁹ The authors predicted that only $\text{Cl}(^2P_{3/2})$ and $\text{O}(^1D_2)$ fragments [channel (3)] were produced as a result of photodissociation in the continuum region based on a comparison with IO. Analysis of the convergence of the vibronic transitions resulted in the onset wavelength for $\text{Cl}(^2P_{3/2})+\text{O}(^1D_2)$ of $263.01\pm 0.1\text{ nm}(38\,052\text{ cm}^{-1})$.¹⁰ McLoughlin *et al.* studied the high-resolution absorption spectrum of ClO using laser absorption spectroscopy.¹¹ The authors estimated the onset wavelength for $\text{Cl}(^2P_{3/2})+\text{O}(^1D_2)$ to be $262.90\pm 0.05\text{ nm}$.

Photodissociation at wavelengths longer than the $\text{O}(^1D_2)$ threshold involves predissociation of the bound $A\ ^2\Pi_\Omega$ state via several repulsive states. Predissociation lifetimes for specific vibrational levels of the $A\ ^2\Pi_\Omega$ state predissociation based on spectral linewidths have been previously reported.^{11–13} A theoretical treatment of the predissociation was first made by Bunker and Klein.¹⁴ The authors neglected a rotational contribution to the predissociation lifetime and predicted predissociation rates using the spin-orbit interaction between $A\ ^2\Pi_\Omega$ state and a single repulsive state corre-

^{a)}Fax: 979-845-2971. Electronic mail: swnorth@tamu.edu

lating to ground-state atoms. The authors concluded that more than a single repulsive state must be involved to explain the observed oscillatory pattern of predissociation lifetimes with wavelength. Recently, Toniolo *et al.* and Lane *et al.* performed high-level *ab initio* calculations of the excited states of ClO and identified several states involved in predissociation of $A^2\Pi_{\Omega}$ state.^{15,16} Both studies concluded that the $1^4\Sigma^+$, $2^4\Sigma^-$, and $3^2\Pi$ states were the principal states responsible for the predissociation of the $A^2\Pi_{\Omega}$ state. Lane *et al.* predicted predissociation lifetimes ranging from 0.5 to 10 ps depending on the $A^2\Pi_{\Omega}$ vibrational level.

In contrast to the numerous spectroscopic studies, there have been a limited number of direct experimental studies of ClO photodissociation. Davis and Lee investigated the photodissociation of ClO at 248 nm using photofragment translational spectroscopy and concluded that channel (3) was the dominant channel (97%) with a minor contribution from channels (1) and (2).¹⁷ The measured nonlimiting anisotropy parameter of 1.2 ± 0.2 for channel (3) suggested that one or more perpendicular transitions contribute significantly (30%) to the oscillator strength at this wavelength. Zou *et al.* studied the photodissociation of ClO near 235 nm using 2+1 resonance-enhanced multiphoton ionization (REMPI) with time-of-flight mass spectrometry (TOFMS).¹⁸ The authors reported that channel (3) was the dominant channel with anisotropy parameter of 1.2 ± 0.2 , suggesting that the photodissociation dynamics of ClO at 230–250 nm is not strongly wavelength dependent. Schmidt *et al.* investigated photodissociation of ClO over the wavelength range of 205–270 nm employing 2+1 REMPI detection of $O(^1D_2)$.¹⁹ Only the sum of channels (3) and (4) in the continuum region was reported since the authors were unable to distinguish between the coincident $Cl(^2P_{3/2})$ and $Cl(^2P_{1/2})$ fragments due to insufficient velocity resolution of the mass spectrometer. They also determined the wavelength corresponding to the onset of the continuum to be 263.4 ± 0.2 nm based on the wavelength-dependent $O(^1D_2)$ yield near threshold. Recently, Flesch *et al.* employed single-photon ionization in the wavelength range of 262–265 nm and determined the $O(^1D_2)$ threshold to be 263.71 ± 0.01 nm.²⁰

In this paper, we report the wavelength-dependent photodissociation dynamics of ClO from 235 to 291 nm corresponding to the wavelengths above, near, and below the $O(^1D_2)$ formation threshold using velocity map ion imaging. In Sec. III A, photodissociation of ClO above the $O(^1D_2)$ threshold is addressed. Here we focus on the identification of photoproducts and angular distributions to unravel the role of excited states other than the $A^2\Pi_{\Omega}$ state and the role of nonadiabatic curve crossing of ClO. Our discussion relies heavily on the recent theoretical work of Persico. In Sec. III B, we present an accurate determination of the $O(^1D_2)$ formation threshold wavelength and discuss the observed breakdown of the axial recoil approximation. In Sec. III C, we examine the state-selected predissociation lifetimes based on the analysis of the photofragment angular distributions and discuss the $Cl(^2P_{3/2})/Cl(^2P_{1/2})$ branching ratio below the $O(^1D_2)$ threshold.

II. EXPERIMENT

A pulsed ClO molecular beam, collimated by a conical skimmer, was intersected at 90° by two copropagating linearly polarized laser beams. The dissociation beam was generated using a 10 Hz Nd:yttrium aluminum garnet (YAG) (Spectra Physics GCR-150-10) pumped dye laser (LAS LDL 2051) operating on the dye Coumarin 500 followed by a frequency doubling crystal [beta-barium borate (BBO)]. The fundamental dye outputs were accurately calibrated using a Ne-filled hollow cathode lamp. The probe beam wavelengths were provided by mixing 1064 nm with the frequency-doubled dye output from a second dye laser (Quantel TDL-51) running on the dye mixture of Rhodamin 610 and 640. A photoelastic modulator (PEM-80, HINDS) was used to rotate the polarization of the probe beam. Typical dissociation and probe pulse energies were 30 and 50 μ J, respectively. The time delay between the dissociation and the probe beam was set to 10 ns in order to detect fast fragments traveling perpendicular to the laser propagation direction. The chlorine atoms [$Cl(^2P_{3/2})/Cl(^2P_{1/2})$] were probed using 2+1 REMPI transitions at 235.336 nm ($4p^2D_{3/2}\leftarrow 3p^2P_{3/2}$) and 235.205 nm ($4p^2P_{1/2}\leftarrow 3p^2P_{1/2}$), respectively.²¹ The oxygen atoms were probed using 2+1 REMPI transitions near 226 nm ($3p^3P_{2,1,0}\leftarrow 2p^3P_{2,1,0}$).²² The resulting chlorine and oxygen ions were accelerated by velocity mapping ion optics pioneered by Eppink and Parker, a variant of traditional ion imaging developed by Chandler and Houston,²³ before entering the 50-cm-long field-free flight tube along the axis defined by the molecular beam.²⁴ The voltages of ion optics were adjusted until the speed resolution of the fragment was maximized. The ions were projected on the position-sensitive microchannel plate phosphor assembly gated to detect the mass of interest. A photomultiplier (PMT) positioned off-axis was used to record mass spectra and establish proper timing. A charge-coupled device (CCD) camera (Mintron MS-2821E/C) acquired images of the phosphor screen and sent raw images to a frame grabber controlled by commercial software (CODA32) which involved centroiding and event counting.²⁵ The final images were obtained by repeatedly scanning Doppler profiles of $Cl(^2P_{3/2})/Cl(^2P_{1/2})$ to achieve homogeneous detection efficiency. Since cylindrical symmetry with respect to the electric field was maintained throughout the experiments, the two-dimensional projections were reconstructed to the original three-dimensional ion spheres by applying the basis-set expansion (BASEX) method developed by Drinbinski *et al.*²⁶

In our previous work on ClO photodissociation the radicals were generated using a pulsed electric discharge^{27,28} similar to the approach of Cooper *et al.*^{18,29} We find that an intense molecular beam of ClO radicals can be generated using the flash pyrolysis of a Cl_2O/He mixture. The active region of the pyrolysis source consists of a 3 cm alumina tube wrapped with nickel-chrome alloy wire which is resistively heated to approximately 800 K.³⁰ Figure 1 demonstrates the production of ClO radicals using the pyrolytic source. The images were collected using one color near 235 nm to probe the $Cl(^2P_{3/2})$ fragments. At room temperature the $Cl(^2P_{3/2})$ image is consistent with Cl_2O photodisso-

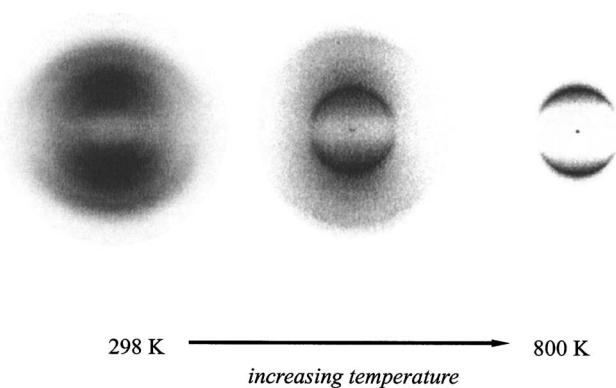


FIG. 1. $\text{Cl}(^2P_{3/2})$ images collected as a function of source temperature. The center spot in the rightmost image is due to entrained Cl atoms from the pyrolysis of Cl_2O .

ciation at 235 nm.³¹ As the nozzle is heated, features associated with Cl_2O decrease in intensity and are replaced by a sharp ring consistent with diatomic photodissociation. At higher temperatures there is little evidence of Cl_2O photodissociation and a bright spot in the center image from entrained Cl atoms is observed. Although the pyrolysis of Cl_2O should, by simple stoichiometry, provide a 1:1 yield of ClO and Cl in the expansion, we find that the relative signals associated with these two species vary greatly depending on the experimental conditions. This is due, in part, to the difference in the rate constants for the reaction of these species with Cl_2O . The reaction of Cl_2O with Cl is rapid ($k=7.3 \times 10^{-11} \text{ cm}^3 \text{ s}^{-1}$ at 800 K),³²



and results in a net loss of Cl and net production of ClO, while the reaction of ClO with Cl_2O is considerably slower.³³ In addition, since the entrained Cl atoms are limited to a few pixels in the center of the image, intense signals can result in attenuation using ion-counting techniques. We find that the formation of hot ClO radicals is significantly reduced by using a water-cooled endcap located at the nozzle tip prior to expansion. Based on images taken near the threshold for $\text{O}(^1D)$ production from ClO (*vide infra*) we estimate that the ClO radicals can be characterized by $T_{\text{rot}} < 100 \text{ K}$, $T_{\text{vib}} < 200 \text{ K}$, and $T_{\text{elec}} < 200 \text{ K}$.

Cl_2O was synthesized by the method of Cady.³⁴ Cl_2 was collected on prebaked HgO (Aldrich) powder and the reaction was allowed to run overnight at 195 K. The product was then purified by vacuum distillation, and the purity (>90%) was checked by UV absorption spectroscopy.

III. RESULTS AND DISCUSSION

A. Photodissociation of ClO above the $\text{O}(^1D_2)$ threshold

The one-color photodissociation of ClO at 235 nm resulted in $\text{Cl}(^2P_{3/2})$ and $\text{Cl}(^2P_{1/2})$ images, as shown in Fig. 2. The speeds of the atomic fragments corresponding to each asymptotic channel can be obtained from the total translational energy of the photofragments by energy conservation

$$E_{\text{trans}}^{\text{total}} = h\nu + E_{\nu,J,e}^{\text{ClO}} - D_0(\text{ClO}) - E_e^{\text{Cl}} - E_e^{\text{O}}, \quad (6)$$

where $h\nu$ is the energy of dissociation photon, $D_0(\text{ClO})$ is the bond energy of ClO, E_e^{Cl} and E_e^{O} are the electronic energy of Cl and O, and $E_{\nu,J,e}^{\text{ClO}}$ is the initial energy of the ClO prior to dissociation which is a function of both Franck-Condon factors and the internal temperature. The accurate determination of the ClO internal temperature and bond dissociation energy will be discussed in the following section. The $\text{Cl}(^2P_{3/2})$ image in Fig. 2 shows a single ring with a speed consistent with the $\text{Cl}(^2P_{3/2}) + \text{O}(^1D_2)$ channel. No evidence for the $\text{Cl}(^2P_{3/2}) + \text{O}(^3P_J)$ channel is observed, consistent with the earlier work of Zou *et al.* In contrast, the $\text{Cl}(^2P_{1/2})$ image shows two rings with speeds consistent with the $\text{Cl}(^2P_{1/2}) + \text{O}(^1D_2)$ and $\text{Cl}(^2P_{1/2}) + \text{O}(^3P_J)$ channels. The signals associated with $\text{Cl}(^2P_{1/2})$ are weak, indicating that the contributions of the $\text{Cl}(^2P_{1/2}) + \text{O}(^1D_2)$ and $\text{Cl}(^2P_{1/2}) + \text{O}(^3P_J)$ channels at 235 nm are minor. We obtained a quantitative branching ratio of $\text{Cl}(^2P_{3/2})$ and $\text{Cl}(^2P_{1/2})$ at 235 nm by integrating Doppler profiles of 2+1 REMPI transitions collected at the identical laser power. The integrated signals are calibrated by using the detection efficiency of $\text{Cl}(^2P_{3/2})$ and $\text{Cl}(^2P_{1/2})$.^{35,36} We find a $\text{Cl}(^2P_{1/2})/\text{Cl}(^2P_{3/2})$ ratio of 0.02 ± 0.01 in good agreement with our previous work.

We have measured two-color images for ClO photodissociation at several wavelengths from 235 to 262 nm. Figure 3 shows the speed distributions of $\text{Cl}(^2P_{3/2})$ (bottom panel) and $\text{Cl}(^2P_{1/2})$ (top panel) derived from images acquired at 255 nm. The solid lines represent forward-convolution simulations to the data (circles) and the arrows in the figure indicate the speeds associated with the various dissociation channels. We do not observe the $\text{Cl}(^2P_{1/2}) + \text{O}(^1D_2)$ channel at 255 nm but observe a small yield of $\text{Cl}(^2P_{3/2}) + \text{O}(^3P_J)$. We have not attempted to measure the relative yields of the oxygen spin-orbit states. The measured $\text{Cl}(^2P_{3/2})$ and $\text{Cl}(^2P_{1/2})$ speed distributions provide accurate relative branching ratios between the $\text{O}(^1D_2)$ and $\text{O}(^3P_J)$ channels coincident with either $\text{Cl}(^2P_{3/2})$ or $\text{Cl}(^2P_{1/2})$. Determination of the relative branching between $\text{Cl}(^2P_{3/2})$ and $\text{Cl}(^2P_{1/2})$ channels proved more difficult since the $\text{Cl}(^2P_{1/2})$ channels are produced in minor yield ($\sim 1\% - 3\%$). We do not observe a significant variation in this yield with wavelength above the $\text{O}(^1D_2)$ threshold based on a comparison of features associated with the photodissociation at a given wavelength with features associated with dissociation by the 235 nm probe in the $\text{Cl}(^2P_{3/2})$ and $\text{Cl}(^2P_{1/2})$ images. We have fixed this value at 0.02 based on our measurements at 235 nm for the results presented in Table I. A comparison to the work of Davis and Lee at 248 nm, where the neutral TOF technique permits an accurate measurement of the $\text{O}(^1D_2)/\text{O}(^3P_J)$ branching ratio, demonstrates that a wavelength-independent $\text{Cl}(^2P_{1/2})/\text{Cl}(^2P_{3/2})$ branching ratio is reasonable. There are several conclusions regarding the relative product yields, however, that do not depend on the absolute $\text{Cl}(^2P_{1/2})/\text{Cl}(^2P_{3/2})$ branching ratio: (1) The yield of $\text{O}(^3P_J)$ is nonzero above the $\text{O}(^1D_2)$ threshold, decreasing from a maximum value of 0.06 at 262 nm to 0.01 at 235 nm. (2) The $\text{Cl}(^2P_{3/2}) + \text{O}(^3P_J)$ channel is not observed at wavelengths shorter than 248 nm and the relative yield of this

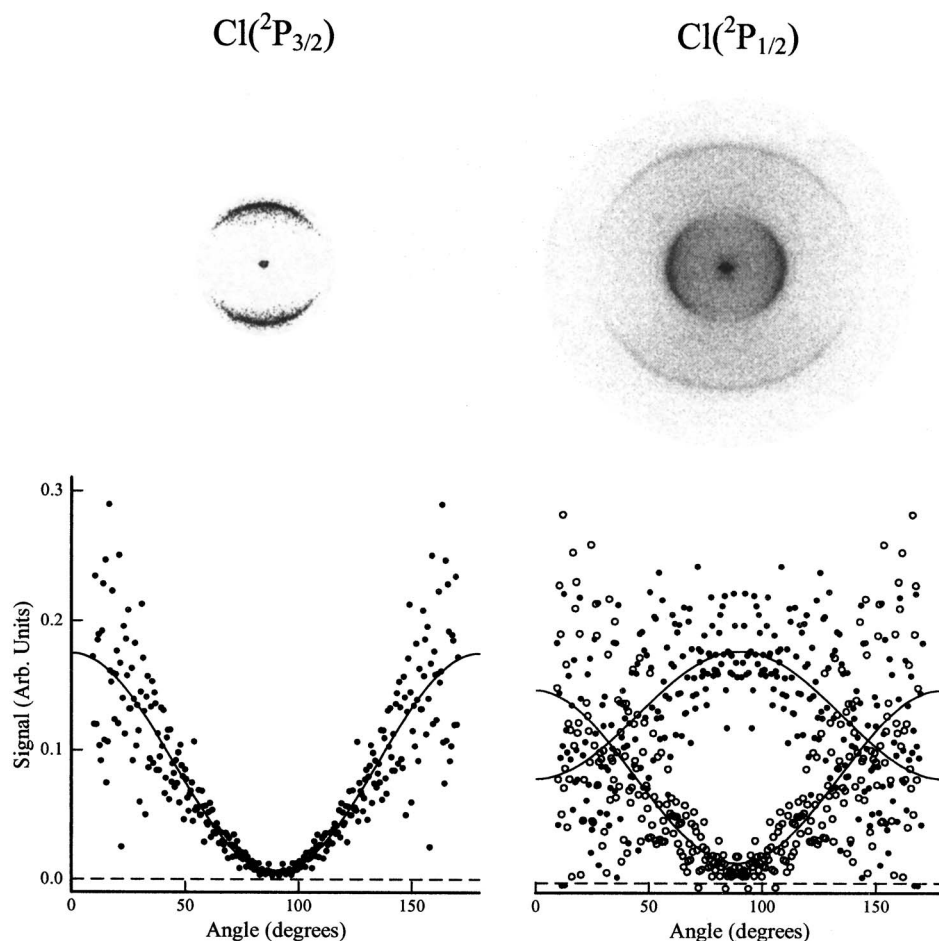


FIG. 2. The upper panel shows raw ion images of $\text{Cl}(^2P_{3/2})$ (left) and $\text{Cl}(^2P_{1/2})$ (right) acquired at 235 nm. The lower panels show the corresponding angular distributions. The solid lines are the best-fit simulations obtained using Eq. (7) in the text.

channel increases with wavelength. (3) The $\text{Cl}(^2P_{1/2}) + \text{O}(^1D_2)$ channel is not observed at wavelengths longer than 248 nm and the relative yield of this channel decreases with wavelength.

The angular distributions of the $\text{Cl}(^2P_{3/2})$ and $\text{Cl}(^2P_{1/2})$ fragments at 235 nm are shown in the lower panel of Fig. 2 and the experimental angular distributions are fitted to the following equation,³⁷

$$I(\theta) = \frac{1}{4\pi} [1 + \beta P_2(\cos \theta)], \quad (7)$$

where β is the spatial anisotropy parameter, $P_2(\cos \theta)$ is the second Legendre polynomial, and θ is the angle between the fragment recoil direction and laser polarization direction. We find best-fit anisotropy parameters of 1.9 ± 0.1 for the $\text{Cl}(^2P_{3/2}) + \text{O}(^1D_2)$ channel, -1.0 ± 0.1 for the $\text{Cl}(^2P_{1/2}) + \text{O}(^1D_2)$ channel, and 1.4 ± 0.1 for the $\text{Cl}(^2P_{1/2}) + \text{O}(^3P_2)$ channel. The anisotropy parameters for the four dissociation channels above $\text{O}(^1D_2)$ threshold are provided in Table I. We did not observe any evidence for orbital alignment of the $\text{Cl}(^2P_j)$ fragments. There was no appreciable difference in the measured anisotropies when the polarization of the probe laser was aligned parallel or perpendicular to the photodissociation laser. We found, however, that the ClO rotational temperature was a sensitive function of nozzle temperature

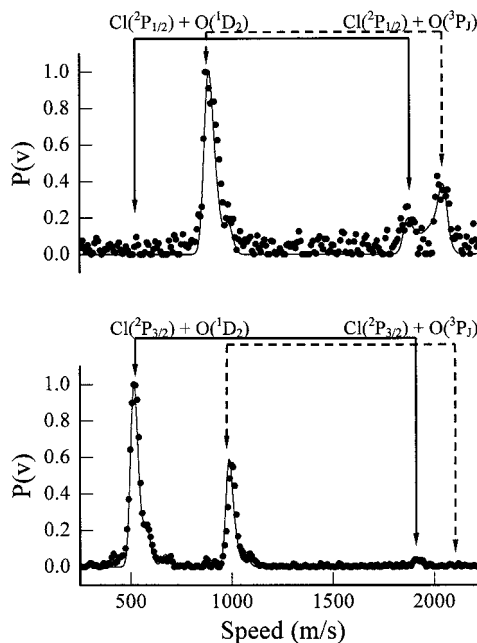


FIG. 3. Speed distributions derived from $\text{Cl}(^2P_{3/2})$ (bottom panel) and $\text{Cl}(^2P_{1/2})$ (top panel) ion images for ClO photodissociation at 235 nm. The arrows indicate the speeds associated with the formation of specific product channels. The dashed lines indicate the speeds associated with the 235 nm probe laser photodissociation.

TABLE I. Summary of relative quantum yields and anisotropy parameters for the ClO photodissociation above the $O(^1D_2)$ threshold.

Wavelength (nm)	$Cl(^2P_{3/2})+O(^3P_j)$		$Cl(^2P_{1/2})+O(^3P_j)$		$Cl(^2P_{3/2})+O(^1D_2)$		$Cl(^2P_{1/2})+O(^1D_2)$	
	Φ	β	Φ	β	Φ	β	Φ	β
235	0.00	...	0.01	1.5	0.98	1.9	0.01	-1
240	0.00	...	0.01	1.1	0.98	1.6	0.01	-1
244	0.00	...	0.02	0.7	0.98	1.9	0.00	-1
248	0.02	0.2	0.02	0.8	0.96	1.7	0.00	...
255	0.03	0.2	0.02	0.9	0.95	1.8	0.00	...
260	0.03	0.1	0.02	1.0	0.95	1.8	0.00	...
262	0.04	0.1	0.02	1.3	0.94	1.7	0.00	...

and the pulsed valve conditions and that photodissociation channels involving the $O(^1D_2)$ result in recoil velocities low enough that rotational depolarization is expected and observed. This effect is especially pronounced near the $O(^1D)$ threshold (*vide infra*). In order to extract intrinsic anisotropy parameters for these channels we fit only the leading edge of the peaks corresponding to the lowest ClO rotational states. This resulted in anisotropy parameters closer to the limiting values than anisotropy parameters averaged over the entire speed distribution. The photodissociation channels corresponding to the $O(^3P_j)$ production result in larger recoil velocities and the measured anisotropy parameters are not as sensitive to parent rotational state. Thus, for these channels the analysis involved an average over the entire velocity distribution.

Davis and Lee measured a nonlimiting anisotropy parameter of 1.2 ± 0.2 for the dominant $Cl(^2P_{3/2})+O(^1D_2)$ channel at 248 nm which is lower than the present result. The authors attributed this low anisotropy parameter to the $2^2\Sigma^+$ state which would be required to carry $\sim 30\%$ of the oscillator strength at this wavelength. Such a large contribution of the $2^2\Sigma^+$ state is inconsistent with theoretical calculations which suggest that this state makes a minor contribution ($< 1\%$) at this wavelength. We have also previously reported a nonlimiting anisotropy parameter of 1.2 ± 0.2 for this channel at 235 nm. We believe that the low value reported in our previous work arose, in part, from the large entrained atomic signal which made analysis of the core-sampled TOF spectra difficult.

Although both the $2^2\Sigma^+$ and $A^2\Pi$ states diabatically correlate to $O(^1D_2)$ products, we find strong evidence for the role of the $2^2\Sigma^+$ state in the dissociation. The minor $Cl(^2P_{1/2})+O(^1D_2)$ channel has an anisotropy parameter of -1.0 ± 0.1 which is consistent with excitation to the $2^2\Sigma^+$ state via a perpendicular transition ($\Delta\Omega = \pm 1$). An alternative source of these fragments could be curve crossing from another state reached via a perpendicular transition. The wavelength-dependent yield of the $Cl(^2P_{1/2})+O(^1D_2)$ channel, assuming that these products arise from direct dissociation of the $2^2\Sigma^+$ state, is in good agreement with the previous theoretical study and is therefore a more likely explanation. Toniolo *et al.* conclude that absorption to this state occurs from 210 to 242 nm, contributing approximately 2.5% of the oscillator strength in this wavelength range. Fig-

ure 4 summarizes the wavelength-dependent branching between channels (1)–(4) above the $O(^1D_2)$ threshold.

Since the $A^2\Pi$ state is the only state with appreciable oscillator strength that is reached via parallel transition ($\Delta\Omega=0$) and this state diabatically correlates to $O(^1D_2)$ products, any curve crossing (adiabatic behavior) will result in $O(^3P_j)$ products with an anisotropy parameter of 2.0. Thus, the cumulative crossing probability from the $A^2\Pi$ state to the $3^2\Pi$, $1^2\Delta$, and $2^4\Sigma^-$ states can be determined by measuring the parallel component to the channels resulting in $O(^3P_j)$ production relative to the total parallel contribution at each wavelength. Based on this analysis and the data provided in Table I, the curve crossing probability decreases from a maximum value of 2% at 262 nm to $< 0.2\%$ at 244 nm, as shown in Fig. 5. This decrease derives primarily from the overall decrease in the $O(^3P_j)$ fragments. We note that both the magnitudes and wavelength dependence are consistent with the theoretical work of Persico. It is not possible, however, to obtain curve crossing probabilities between *specific* states and $A^2\Pi$ state to compare with theory. The perpendicular contribution to the $O(^1D_2)$ channels could, in principle, permit a determination of the curve crossing probability to the $A^2\Pi$ from other states. Although less than limiting values for the anisotropy parameter are observed for the dominant $Cl(^2P_{3/2})+O(^1D_2)$ channel, this variation most likely reflects uncertainties in the anisotropy measurements rather than very large curve crossing probabilities from states reached via a perpendicular transition.

B. Photodissociation of ClO near the $O(^1D_2)$ threshold

We have investigated the photodissociation dynamics of ClO at wavelengths near the $O(^1D_2)$ threshold. The formation of Cl atoms in coincidence with $O(^1D_2)$ in this region results in little translational energy. As a result, the measured speed distributions are extremely sensitive to the available energy, i.e., the precise value of the Cl–O bond dissociation energy and the initial energy content of the ClO radicals. The lower panel of Fig. 6 shows the $Cl(^2P_{3/2})$ speed distribution derived from the measured image at 262 nm. This wavelength corresponds to excitation just above the $O(^1D_2)$ threshold. At higher speeds, not shown in the figure, we observed a small feature consistent with the formation of coin-

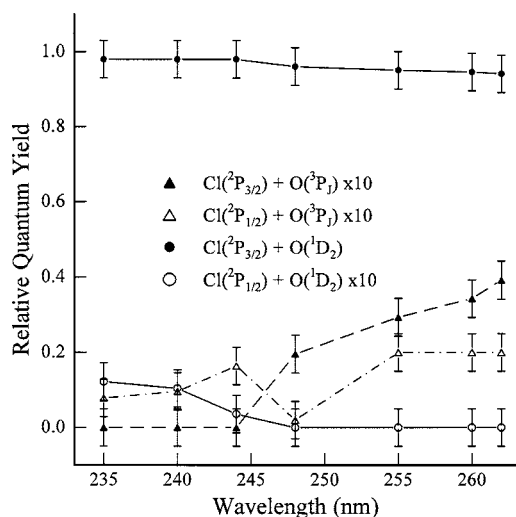


FIG. 4. Wavelength-dependent relative branching ratios of the ClO photodissociation channels. The minor channels have been multiplied by a factor of 10 for clarity.

cident $O(^3P_j)$. The finite width of the measured speed distribution is a reflection of the initial internal state distribution of the ClO radical. The speeds associated with individual ClO rotational levels in both spin-orbit states are indicated by the vertical lines in the figure. The rotational distribution is characterized by a temperature of 100 K and the spin-orbit branching ratio by an electronic temperature of 200 K. We have assumed that the vibrational temperature is <200 K based on a lack of clear signal corresponding to $v=1$ ClO. The line spectrum has been convoluted with a Gaussian ($\sigma = 15$ m/s) to reflect instrumental resolution. The resulting solid line provides a reasonable fit to measured speed distribution. We have assumed a threshold energy of $38\,050 \pm 20$ cm^{-1} for fitting the speed distributions. The fits are extremely sensitive to this value near threshold, both in terms of the absolute speeds and the spacing between peaks

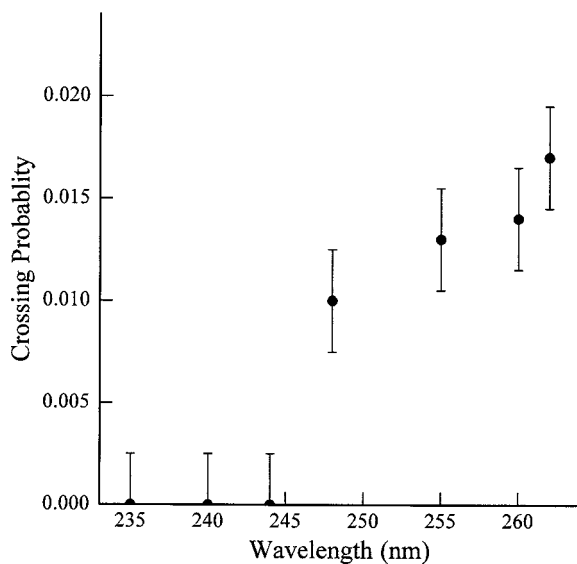


FIG. 5. Cumulative curve crossing probability from the $A\ ^2\Pi$ state to yield $\text{Cl}(^2P_{3/2}) + \text{O}(^3P_j)$ products above the $\text{O}(^1D_2)$ threshold.

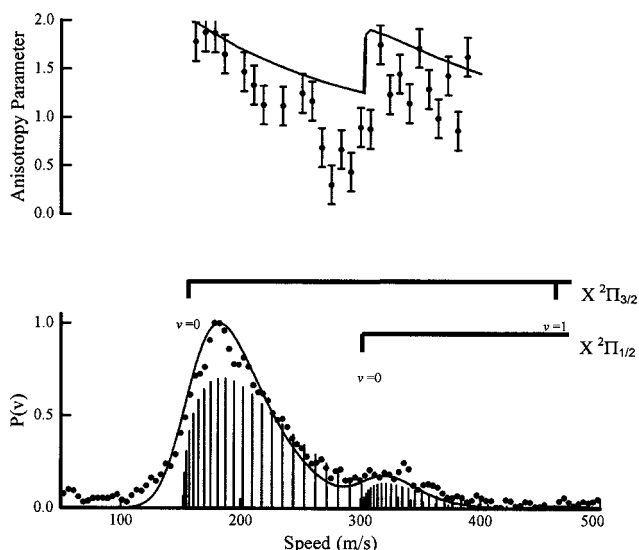


FIG. 6. Speed distribution and speed-dependent anisotropy parameters for $\text{Cl}(^2P_{3/2})$ fragments arising from ClO photodissociation at 262 nm. The bottom panel shows the simulation of the speed distribution using a ClO rotational population of 100 K. The top panel shows the speed-dependent anisotropy parameters. The solid line represents the classical prediction for the anisotropy parameter and the filled circles represent the data.

which correspond to each spin-orbit state fixed at 318 cm^{-1} . The threshold energy was derived from the fits to speed distributions acquired at multiple wavelengths, some below the threshold where the fragments produced arise from ClO radicals with nonzero internal energy.

The speed-dependent anisotropy parameters for the $\text{Cl}(^2P_{3/2})$ fragments are shown in the upper panel of Fig. 6. Excitation in this wavelength region involves a parallel transition to the $A\ ^2\Pi$ state above the $\text{O}(^1D_2)$ threshold followed by direct dissociation. In the axial recoil approximation, where the recoil axis and molecular axis are nearly equivalent, the anisotropy parameter would be near its limiting value of 2. The measured anisotropy parameters, however, are substantially lower than this limiting value. The decrease in anisotropy parameter is due to a breakdown in the axial recoil approximation, i.e., a reorientation of the recoil velocity resulting from initial angular momentum of the parent. Evidence for this effect was reported recently in the near threshold photodissociation of IBr.^{38–40} The breakdown of the axial recoil approximation is expected when the radial and tangential velocities are comparable and the larger the parent rotational state the larger the magnitude of the effect. A comparison of the measured anisotropy parameters with parent rotational states demonstrates that the measurements are consistent with such a trend. In particular, the sudden increase in the anisotropy parameter corresponding to the lowest rotational states of the ClO spin-orbit excited state provides compelling evidence. A more quantitative treatment of the speed-dependent anisotropy parameters can be obtained using a simple classical model. Following the discussion of Wrede *et al.*⁴⁰ the classical motion of a rotating diatomic molecule is described by the effective Hamiltonian, ignoring internal angular momentum,

$$H = V(R) + \frac{p^2}{2\mu} + \frac{J^2}{2\mu R^2} \quad (8)$$

and the relation between the angle of rotation (γ) and internuclear separation can be expressed by solving Hamiltonian's equation of motion

$$\frac{\partial \gamma}{\partial R} = \frac{J}{p(R)R^2}, \quad (9)$$

where the conjugate momentum $p(R)$ is given by

$$p(R) = [2\mu\{E - V(R)\} - J^2/R^2]^{1/2}. \quad (10)$$

In Eq. (10), J is the rotational angular momentum, $V(R)$ is a Morse potential describing the $A^2\Pi$ state, and E is the photon energy. The molecular constants of the $X^2\Pi$ state and $A^2\Pi$ state potential curves were obtained from previous spectroscopic results.⁴¹

The final angle of rotation is given by

$$\gamma = \int_{R_0}^{\infty} \frac{JdR}{p(R)R^2}, \quad (11)$$

where R_0 is the turning point of the Morse potential at the corresponding excitation energy. Although the choice of the inner turning point as the initial condition for the classical trajectory is an oversimplification, the repulsive wall of the $A^2\Pi$ state lies nearly directly above the ground-state minimum at excitation energies near the $O(^1D_2)$ threshold.

The azimuthally averaged addition theorem⁴² permits the anisotropy parameter to be written as a product of two terms

$$\beta = 2P_2(\cos \chi)P_2(\cos \gamma), \quad (12)$$

where χ is the recoil angle relative to the molecular axis, the second term reflects the reorientation of the recoil axial from the molecular axis by angle γ . The predictions using Eqs. (9)–(12) are shown as the solid lines in the upper panel of Fig. 6. Although there is qualitative agreement with the data the model consistently underestimates the magnitude of the effect. The classical treatment includes the rotational angular momentum of the ClO but ignores orbital angular momentum of both ClO and the angular momentum of the atomic fragments. A second source of systematic error involves the treatment of low velocities that result in small ion images. Since all the ions are projected on a limited number of pixels, the derived anisotropy parameters will be more isotropic than the intrinsic angular distribution although our simulations indicate that the effect is small in agreement with the conclusions reached by Wrede *et al.*

Based on the analysis of the images discussed previously we have established both the energy of the threshold ($38\,050 \pm 20 \text{ cm}^{-1}$) and the internal energy distribution of the ClO radicals. As additional confirmation we have measured the relative $O(^1D_2)$ and $O(^3P_j)$ yields near the threshold. The insets of Fig. 7 show $\text{Cl}(^2P_{3/2})$ images acquired at two wavelengths near threshold. The outer ring in the 265 nm image corresponds to $O(^3P_j)$ formation arising from the predissociation below threshold. The inner ring in the image is due to $O(^1D_2)$ formation and the intermediate ring is from the 235 nm probe laser. In the lower 262 nm image the outer

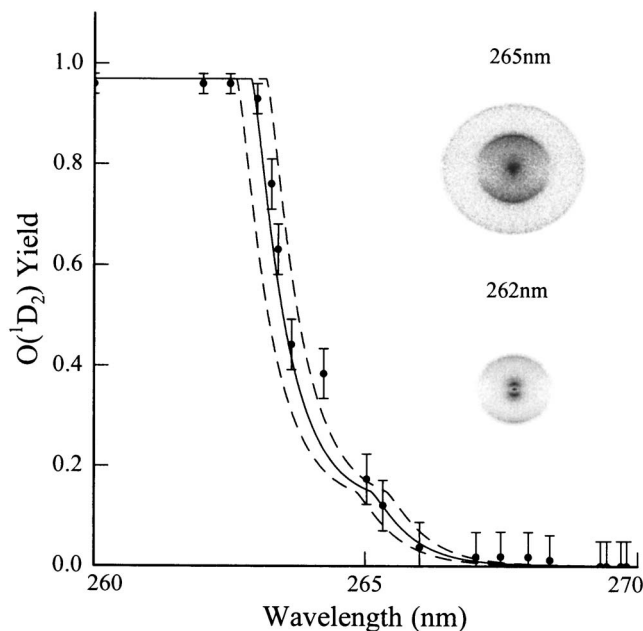


FIG. 7. Wavelength-dependent $O(^1D_2)$ quantum yield over the range of 260–270 nm based on Eq. (13). The outer ring in panel A arises from $\text{Cl}(^2P_{3/2})$ in coincidence with $O(^3P_j)$ at 265 nm: the inner and intermediate rings in the middle are due to $\text{Cl}(^2P_{3/2}) + O(^1D_2)$ at 235 and 265 nm, respectively. In panel B, two rings that can be observed arise from $\text{Cl}(^2P_{3/2}) + O(^1D_2)$ at 235 nm (outer ring) and 262 nm (inner ring), respectively.

ring is very weak and the innermost ring has increased noticeably in radius. In order to extract relative branching ratios for $O(^1D_2)$ and $O(^3P_j)$ formed in coincidence with $\text{Cl}(^2P_{3/2})$ the wavelength-dependent images were converted to speed distributions and the integrated areas of the peaks associated with each channel were compared. Previous work by Wrede *et al.* has shown that ClO excitation in this wavelength region results in the formation of ion-pair states. We find that photodissociation through these states results in intense Cl^+ and O^+ images. A full description of this process is the subject of future publication. We have selected wavelengths near threshold which avoid these ion-pair states to facilitate analysis. Figure 7 shows a plot of the wavelength-dependent $O(^1D_2)$ quantum yield near the threshold using

$$\Phi^{\text{Cl}}(O(^1D_2)) = \frac{I(O(^1D_2))}{I(O(^1D_2)) + I(O(^3P_j))}, \quad (13)$$

where $I(O(^1D_2))$ and $I(O(^3P_j))$ represent areas of the peaks in the derived speed distributions corresponding to the $\text{Cl}(^2P_{3/2}) + O(^1D_2)$ and $\text{Cl}(^2P_{3/2}) + O(^3P_j)$ channels, respectively. The data show a dramatic change in the $O(^1D_2)$ yield between 262.5 and 264.5 nm consistent with the energetic threshold for $O(^1D_2)$ formation. The finite width of this onset is the result of nonzero ClO internal energy which allows for $O(^1D_2)$ formation at wavelengths corresponding to energies below the threshold. The solid and dashed lines in the figure represent simulations of the $O(^1D_2)$ fixing the quantum yield for total energies exceeding the threshold at 0.97. It should be noted that the reported $O(^1D_2)$ yields are based only on the $\text{Cl}(^2P_{3/2})$ images. Although above the threshold the $\text{Cl}(^2P_{1/2})$ yield is minor, below threshold we find that the $\text{Cl}(^2P_{3/2})/\text{Cl}(^2P_{1/2})$ ratio is approximately 1.5 and the overall

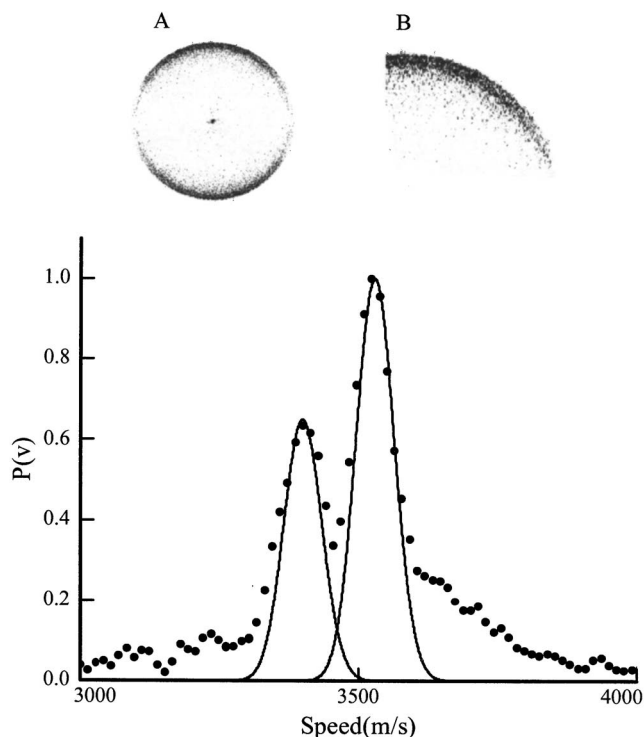


FIG. 8. Panel A shows $O(^3P_2)$ image acquired at 291.71 nm. Panel B is the enlargement of panel A. The lower panel shows an expanded region of the speed distribution derived from the $O(^3P_2)$ image. The slower feature corresponds to the $Cl(^2P_{1/2})+O(^3P_2)$ channel and the faster feature corresponds to the $Cl(^2P_{3/2})+O(^3P_2)$ channel.

$O(^1D_2)$ yields should, therefore, include this correction. As evidence of the $Cl(^2P_{3/2})/Cl(^2P_{1/2})$ branching ratio Fig. 8 shows an $O(^3P_2)$ image acquired at 291.71 nm along with an expanded region of the speed distribution (bottom panel). The $O(^3P_2)$ image exhibits two distinctive rings indicating the evidence of $O(^3P_2)$ in coincidence with $Cl(^2P_{3/2})$ and $Cl(^2P_{1/2})$. Integration of the peaks in the speed distribution results in a branching ratio of $Cl(^2P_{3/2})/Cl(^2P_{1/2})$ of 1.5 ± 0.1 at 291.71 nm. A similar result was obtained from measurements at 266 nm.

The solid line in Fig. 7 corresponds to a threshold energy of $38\,050\text{ cm}^{-1}$ and the dashed lines represent $\pm 40\text{ cm}^{-1}$, assuming the thermal distribution of ClO is characterized by $T_{\text{rot}}=100\text{ K}$, $T_{\text{vib}} < 200\text{ K}$, and $T_{\text{elec}}=200\text{ K}$. We have included the small shift in the onset of individual rovibrational states due to the centrifugal barrier by using a Morse potential for the $A\ ^2\Pi$. The effect is minor, resulting in a correction of only a few cm^{-1} for the largest rotational states. We find that the best-fit value of the threshold for $O(^1D_2)$ formation for fitting the onset data is in excellent agreement with independent fits to the fragment speed distributions. Our result is in excellent agreement with the $38\,052\text{ cm}^{-1}$ reported by Coxon and Ramsay based on the convergence of vibronic transitions.

To date, direct measurement of $O(^1D_2)$ threshold by detection of $O(^1D_2)$ has been performed by two groups. Flesch *et al.* recently employed vacuum ultraviolet (vuv) photoionization detection to measure the $O(^1D_2)$ onset. The authors used a sigmoidal fit to the onset curve and reported a value

of $37\,820 \pm 2\text{ cm}^{-1}$ corresponding to 10% of the maximum $O(^1D_2)$ yield. The apparent redshift of the onset value to our threshold value can be attributed to the ClO thermal energy. In addition, the authors observed a steeper onset curve than anticipated, suggesting the presence of a rotational barrier. However, we fail to detect evidence for such an effect. Schmidt *et al.* made a similar measurement using 2+1 REMPI detection of the $O(^1D_2)$ fragments and reported a value of $37\,965 \pm 30\text{ cm}^{-1}$ corresponding to the cutoff of the $O(^1D_2)$ signal. The value is consistent with a thermal redshift from the energetic threshold. Neither Flesch *et al.* nor Schmidt *et al.* addressed the nonzero yield of $O(^3P_J)$ above the $O(^1D_2)$ threshold or observed evidence for a separate onset due to spin-orbit excited ($A\ ^2\Pi_{1/2}$) ClO. Our approach differs from the previous studies in that each measurement of the $Cl(^2P_{3/2})$ speed distribution provides the yield of both $O(^3P_J)$ and $O(^1D_2)$ and given the resolution of the technique avoids interference from other dissociation channels.

C. Photodissociation of ClO below the $O(^1D_2)$ threshold

In this section we report on our initial investigation of ClO photodissociation below the $O(^1D_2)$ threshold. We focus on the determination of state-selected predissociation lifetimes based on the analysis of photofragment angular distributions and discuss the $Cl(^2P_{3/2})/Cl(^2P_{3/2})$ branching ratio. At wavelengths below $\sim 267\text{ nm}$ only channels (1) and (2), which involve $O(^3P_J)$ fragments, are observed.

The top panel of Fig. 9 shows the wavelength dependence of the anisotropy parameter in the region of 9-0 band (left) and 8-0 band (right) for the $Cl(^2P_{3/2})+O(^3P_J)$ channel. The bottom panel shows spectral simulations of 9-0 band and 8-0 band along with the measured photofragment excitation (PHOFEX) spectra (closed circles), corresponding to the $Cl(^2P_{3/2})+O(^3P_J)$ image features as a function of wavelength. The spectral simulations based on the sum of P , Q , and R branches of the $A\ ^2\Pi_{3/2} \leftarrow X\ ^2\Pi_{3/2}$ transition using molecular constants are obtained from previous spectroscopic results. The simulations are restricted to the $^{35}\text{Cl}^{16}\text{O}$ isotopomer since we detect only $m/z=35$ and we have used a rotational temperature of 100 K. Although the PHOFEX data qualitatively matched the band envelopes we were unable to resolve the rotational structure since the individual images consisted of a limited number of laser shots, necessary to avoid drifts in the source and laser powers. It should be noted that it was necessary to analyze images, rather than the total ion signals, as a function of wavelength in order to distinguish between the true signal and signal due to entrained $Cl(^2P_{3/2})$ atoms or ion-pair signal. The effect of finite lifetime on the anisotropy parameter can be calculated using the following equation:⁴³⁻⁴⁵

$$\beta_{(\tau)} = \beta_{(\tau=0)} \frac{1 + \omega^2 \tau^2}{1 + 4\omega^2 \tau^2}, \quad (14)$$

where τ is the predissociation lifetime, ω is the rotational angular velocity, $\beta_{(\tau)}$ is the observed anisotropy parameter, and $\beta_{(\tau=0)}$ is the intrinsic anisotropy parameter which should be 2.0 for a parallel transition ($A\ ^2\Pi \leftarrow X\ ^2\Pi$). Since the ob-

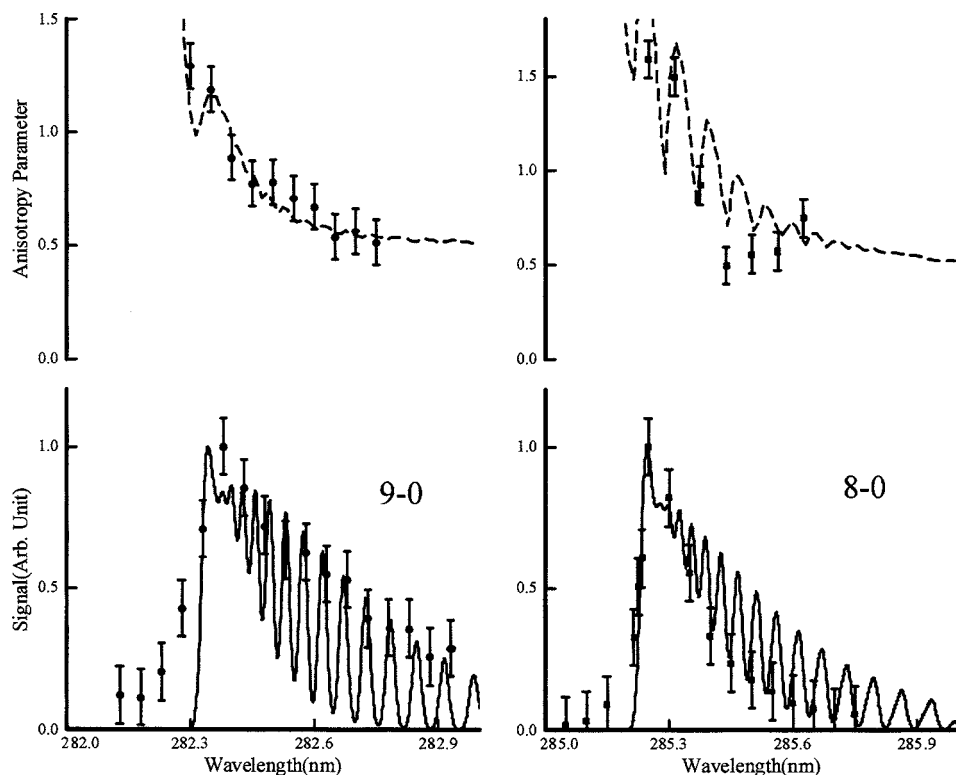


FIG. 9. The bottom panels show the spectral simulations of ^{35}ClO absorption (solid lines) in the region of the 9-0 band (left) and 8-0 band (right) at 100 K. The filled circles represent the relative $\text{Cl}(^2P_{3/2})$ image intensity. The top panels show the measured anisotropy parameters (filled circles) and associated simulations (dashed line) using Eq. (14). The best fits provide predissociation lifetimes of 1.5 ± 0.2 and 1.0 ± 0.4 ps for the 9-0 (left) and the 8-0 (right) bands, respectively.

served anisotropy parameter is very sensitive to rotational state as well as the predissociation lifetime, we measured a series of image intensities across the bandhead to identify the rotational state of ClO.⁴⁶ Lane *et al.* reported that the lifetime broadening showed no dependence on the rotational states, i.e., the predissociation mechanism is dominated by spin-orbit interaction between the $A^2\Pi$ and the dissociative state. Assuming a J' -independent predissociation lifetime, we can fit the wavelength-dependent anisotropy parameters for the 9-0 band and 8-0 band using Eq. (14). The peaks in the lower panels of Fig. 9 represent overlapping $P(J)$ and $R(J+5)$ branch lines and the anisotropy parameters calculated using Eq. (14) represent weighted averages of the excited-state J values. Based on this analysis, and illustrated in the top panels of Fig. 9, we have determined predissociation lifetimes of 1.5 ± 0.2 and 1.0 ± 0.4 ps for the 9-0 and 8-0 bands, respectively. Our results are in reasonable agreement with the lifetimes reported in previous high-resolution spectroscopic studies, as indicated in Table II.¹¹⁻¹³ The differences between the lifetimes estimated using Eq. (14) and the lifetimes reported from line broadening measurements are not unexpected. The derivation of Eq. (14) relies on the coherent excitation of different upper J states via P -, R -, and Q -branch transitions which leads to a classical time evolution in orientation sampled by delayed dissociation. However, the present case is characterized by narrow-band excitation, essentially cw on the time scale of predissociation. The optical selection of individual parent J states (albeit overlapping J states due to P - and R -branch transitions) implies predissociation slow enough to permit partially resolved rotational lines, suggesting that the conditions necessary for the implementation of Eq. (14) are not realized. We are currently pursuing studies aimed at further investigation of the angular distributions

arising from the photodissociation of these resolved bands using imaging of the $\text{O}(^3P_0)$ fragment to provide an unambiguous measure of the spatial anisotropy. A recent high-level *ab initio* study employing Fermi golden rule calculations on the excited states of ClO by Lane *et al.* identified the principal dissociative states that couple to $A^2\Pi_{3/2}$ state. Candidate states for the predissociation of $A^2\Pi$ state were se-

TABLE II. ν -dependent lifetimes for the $A^2\Pi_{3/2}$ states of ClO.

Band	τ^a (ps)	τ^b (ps)	τ^c (ps)	τ^d (ps)
0-0		4.43		
1-0		2.00		
2-0		1.97		
3-0		0.97		
4-0		1.28		
5-0	1.06	0.83		
6-0	1.15	0.53		1.0 ± 0.3
7-0	1.08	1.06	1.02	
8-0	0.92		1.11	1.0 ± 0.4
9-0	2.27		1.03	1.5 ± 0.2
10-0	1.45		0.94	1.0 ± 0.3
11-0	0.98		1.48	
12-0	1.92		1.42	
13-0	2.56			
14-0	2.92			
15-0	5.07			
16-0	3.04			
17-0	13.31			
18-0	10.24			

^aMcLoughlin *et al.* (Ref. 11).

^bHowie *et al.* (Ref. 13).

^cBarton *et al.* (Ref. 12).

^dPresent work.

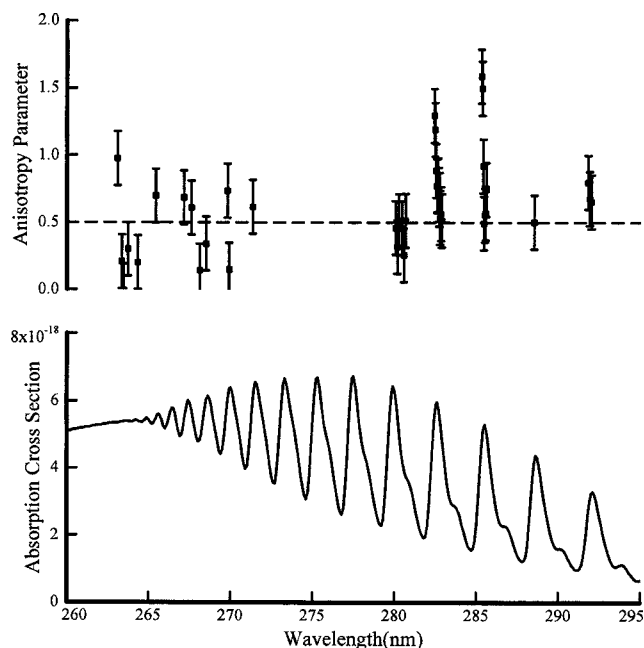


FIG. 10. Wavelength-dependent anisotropy parameters associated with the $\text{Cl}(^2P_{3/2}) + \text{O}(^3P_J)$ channel (top panel). The dashed line is the classical long-time limit based on Eq. (14). The CIO absorption spectrum from Ref. 7 is shown for comparison in the bottom panel.

lected based on electronic configuration arguments. A comparison of the calculated predissociation lifetimes for each vibrational level and to experimental predissociation lifetimes derived from spectroscopic linewidths led the authors to assign the predissociation primarily to the $1^4\Sigma^+$, $2^4\Sigma^-$, and $3^2\Pi$ states.

Figure 10 shows all the anisotropy parameters measured for the $\text{Cl}(^2P_{3/2}) + \text{O}(^3P_J)$ channel below the $\text{O}(^1D_2)$ threshold (upper panel) along with CIO absorption spectrum (bottom panel) taken from Trolier *et al.* The dashed line in the upper panel shows the classical long-time limit predicted by Eq. (14). The variation of anisotropy parameter with wavelength across specific vibronic bands is observed, consistent with Eq. (14) as previously discussed. At wavelengths approaching the $\text{O}(^1D_2)$ threshold the anisotropy parameters for the $\text{Cl}(^2P_{3/2}) + \text{O}(^1D_2)$ channel are far from their limiting value and several lie below the classical limit. The origin of these low anisotropy parameters below ~ 267 nm is due to several factors. There is spectroscopic evidence that these high vibrational states have long predissociation lifetimes (Table II). In addition, at wavelengths shorter than 267 nm the yield of $\text{O}(^3P_J)$ decreases as the $\text{O}(^1D_2)$ channels become energetically accessible and an increasing fraction of the $\text{O}(^3P_J)$ fragments arises from direct dissociation rather than predissociation. Since $\text{O}(^3P_J)$ formation above the threshold has contributions from direct dissociation of states reached via perpendicular transitions (Table I) anisotropy parameters below 0.5 are not unexpected.

IV. CONCLUSIONS

We have investigated the UV photodissociation dynamics of CIO above, near, and below the $\text{O}(^1D_2)$ formation threshold using velocity map ion imaging. We find that

$\text{Cl}(^2P_{3/2}) + \text{O}(^1D_2)$ is the dominant dissociation pathway (>0.94) above $\text{O}(^1D_2)$ threshold with minor contributions from the $\text{Cl}(^2P_J) + \text{O}(^3P_J)$ and $\text{Cl}(^2P_{1/2}) + \text{O}(^1D_2)$ channels. Based on the anisotropy parameter for the $\text{Cl}(^2P_{1/2}) + \text{O}(^1D_2)$ channel we believe that this channel results from direct dissociation of the $2^2\Sigma^+$ state. We observe $\text{O}(^3P_J)$ fragments with positive anisotropy, strong evidence of curve crossing from the $A^2\Pi$ to one of several dissociative states. Both the magnitude and wavelength dependence of the curve crossing probability are in good agreement with the theoretical calculations of Persico. A careful analysis of the speed distribution of $\text{Cl}(^2P_{3/2})$ fragments just above the $\text{O}(^1D_2)$ threshold permits the accurate energetic determination of this threshold of $38\,050 \pm 20$ cm^{-1} . Predissociation lifetimes CIO for selected vibronic bands have been obtained using the rotational depolarization of the photofragment angular distribution. We find values in the range of 1.0–1.5 ps depending on the upper-state vibrational level. We also find that the $\text{Cl}(^2P_{3/2})/\text{Cl}(^2P_{1/2})$ branching ratio is approximately 1.5 ± 0.1 below the $\text{O}(^1D_2)$ threshold based on careful measurements at 266 and 291 nm, respectively.

ACKNOWLEDGMENTS

The authors wish to thank Maurizio Persico for discussions regarding CIO excited states and acknowledge Gregory Hall. The technical assistance of Erin E. Greenwald, Katie Anderson, and Kristin Dooley is gratefully appreciated. One of the authors (S.W.N.) wishes to thank Arthur Suits for his help and support in getting the imaging experiments up and running. Support for this project was provided by the Robert A. Welch Foundation (Grant No. A-1402).

- ¹M. J. Molina and F. S. Rowland, *Nature (London)* **249**, 810 (1974).
- ²R. R. Garcia and S. Solomon, *J. Geophys. Res., [Atmos.]* **99**, 12937 (1994).
- ³S. Solomon, R. R. Garcia, F. S. Rowland, and D. J. Wuebbles, *Nature (London)* **321**, 755 (1986).
- ⁴P. O. Wennberg, R. C. Cohen, R. M. Stimpfle *et al.*, *Science* **266**, 398 (1994).
- ⁵P. Zou, J. Park, B. A. Schmitz, T. Nguyen, and S. W. North, *J. Phys. Chem. A* **106**, 1004 (2002).
- ⁶H. Kim, E. E. Greenwald, J. Park, and S. W. North (unpublished).
- ⁷M. Trolier, R. L. Mauldin III, and A. R. Ravishankara, *J. Phys. Chem.* **94**, 4896 (1990).
- ⁸E. Wigner and E. E. Witmer, *Z. Phys.* **51**, 859 (1928).
- ⁹R. A. Durie and D. A. Ramsay, *Can. J. Phys.* **36**, 35 (1958).
- ¹⁰J. A. Coxon and D. A. Ramsay, *Can. J. Phys.* **54**, 1034 (1976).
- ¹¹P. W. McLoughlin, C. R. Park, and J. R. Wiesenfeld, *J. Mol. Spectrosc.* **162**, 307 (1993).
- ¹²S. A. Barton, J. A. Coxon, and U. K. Roychowdhury, *Can. J. Phys.* **62**, 473 (1984).
- ¹³W. H. Howie, I. C. Lane, S. M. Newman, D. A. Johnson, and A. J. Orr-Ewing, *Phys. Chem. Chem. Phys.* **1**, 3079 (1999).
- ¹⁴P. R. Bunker and P. C. Klein, *Chem. Phys. Lett.* **78**, 552 (1981).
- ¹⁵A. Toniolo, M. Persico, and D. Pitea, *J. Chem. Phys.* **112**, 2790 (2000).
- ¹⁶I. C. Lane, W. H. Howie, and A. J. Orr-Ewing, *Phys. Chem. Chem. Phys.* **1**, 3086 (1999).
- ¹⁷H. F. Davis and Y. T. Lee, *J. Phys. Chem.* **100**, 30 (1996).
- ¹⁸P. Zou, H. Kim, and S. W. North, *J. Chem. Phys.* **116**, 4176 (2002).
- ¹⁹S. Schmidt, Th. Benter, and R. N. Schindler, *Chem. Phys. Lett.* **282**, 292 (1998).
- ²⁰R. Flesch, J. Plenge, S. Kühl, M. Klusmann, and E. Rühl, *J. Chem. Phys.* **117**, 9663 (2002).

- ²¹ S. Arepalli, N. Presser, D. Robie, and R. J. Gordon, *Chem. Phys. Lett.* **117**, 64 (1985).
- ²² D. J. Banford, L. E. Jusinsk, and W. K. Bischel, *Phys. Rev. A* **34**, 185 (1986).
- ²³ D. W. Chandler and P. L. Houston, *J. Chem. Phys.* **87**, 1445 (1987).
- ²⁴ A. T. Eppink and D. H. Parker, *Rev. Sci. Instrum.* **68**, 3447 (1997).
- ²⁵ B.-Y. Chang, R. C. Hoetzlein, J. A. Mueller, J. D. Geisler, and P. L. Houston, *Rev. Sci. Instrum.* **69**, 1665 (1998).
- ²⁶ V. Drinbinski, A. Ossadtchi, V. A. Mandelshtam, and H. Reisler, *Rev. Sci. Instrum.* **73**, 2634 (2002).
- ²⁷ D. T. Anderson, S. Davis, T. S. Zwier, and D. J. Nesbitt, *Chem. Phys. Lett.* **258**, 207 (1996).
- ²⁸ M. C. van Beek and J. J. ter Meulen, *Chem. Phys. Lett.* **337**, 237 (2001).
- ²⁹ M. J. Cooper, T. Diez-Rojo, L. J. Rogers, C. M. Western, M. R. N. Ashfold, and J. W. Hudgens, *Chem. Phys. Lett.* **272**, 232 (1997).
- ³⁰ We predict a rate constant for the $\text{Cl}_2\text{O} \rightarrow \text{ClO} + \text{Cl}$ reaction at 700 K of $2.3 \times 10^4 \text{ s}^{-1}$ corresponding to a Cl_2O lifetime close to the transit time through the heated nozzle.
- ³¹ Y. Tanaka, M. Kawasaki, Y. Matsumi, H. Fujiwara, T. Ishiwata, L. J. Rogers, R. N. Dixon, and M. A. R. Ashfold, *J. Chem. Phys.* **109**, 1315 (1998).
- ³² W. B. DeMore, S. P. Sander, D. M. Golden, R. F. Hampson, M. J. Kurylo, C. J. Howard, A. R. Ravishankara, C. E. Kolb, and M. J. Molina, *JPL Publ.* **97-4**, 29 (1997).
- ³³ N. Basco and S. K. Dogra, *Proc. R. Soc. London, Ser. A* **323**, ■ (1971).
- ³⁴ G. H. Cady, *Inorg. Synth.* **9**, 127 (1967).
- ³⁵ M. Ahmed, D. Blunt, D. Chen, and A. G. Suits, *J. Chem. Phys.* **106**, 7617 (1997).
- ³⁶ J. Zhang, M. Dulligan, and C. Wittig, *J. Chem. Phys.* **107**, 1403 (1997).
- ³⁷ R. N. Zare, *Mol. Photochem.* **4**, 1 (1972).
- ³⁸ E. Wrede, S. Laubach, S. Schulenburg, A. J. Orr-Ewing, and M. N. R. Ashfold, *Chem. Phys. Lett.* **326**, 22 (2000).
- ³⁹ E. Wrede, S. Laubach, S. Schulenburg, A. Brown, E. R. Wouters, A. J. Orr-Ewing, and M. N. R. Ashfold, *J. Chem. Phys.* **114**, 2629 (2001).
- ⁴⁰ E. Wrede, E. R. Wouters, M. Beckert, R. N. Dixon, and M. N. R. Ashfold, *J. Chem. Phys.* **116**, 6064 (2002).
- ⁴¹ K. P. Huber and G. Hertzberg, *Constants of Diatomic Molecules* (Van Nostrand, New York, 1979).
- ⁴² J. D. Barnwell, J. G. Loesser, and D. R. Hershbach, *J. Phys. Chem.* **87**, 2781 (1983).
- ⁴³ C. Jonah, *J. Chem. Phys.* **55**, 1915 (1971).
- ⁴⁴ G. E. Busch and K. R. Wilson, *J. Chem. Phys.* **56**, 3638 (1972).
- ⁴⁵ S. Yang and R. Bersohn, *J. Chem. Phys.* **61**, 4400 (1974).
- ⁴⁶ As an additional check that there is no significant orbital alignment of the $\text{Cl}(^2P_{3/2})$ fragments we have compared the anisotropy derived from $\text{Cl}(^2P_{3/2})$ images taken at 266 nm with the anisotropy derived from the $\text{O}(^3P_0)$ image, which cannot be distorted by alignment, at the same wavelength. We find that the anisotropy parameters are equivalent within the mutual error bars.